Nuclear Science and Techniques (2026) 37:92
https://doi.org/10.1007/s41365-026-01918-1

An effective method toward large field-of-view gamma-ray computed tomography based on an inverse Compton scattering light source

Zhi-Jun Chi[1] · Hong-Ze Zhang[2] · Jia-Yi Sun[2] · Hao Ding[2] · Jin Lin[2] · Xuan-Qi Zhang[2] · Qi-Li Tian[2] · Zhi Zhang[2] · Ying-Chao Du[2] · Wen-Hui Huang[2] · Chuan-Xiang Tang[2]

Received: 18 July 2024 / Revised: 7 December 2024 / Accepted: 16 December 2024 / Published online: 12 March 2026

Abstract
The quasi-monochromatic, continuously energy-tunable, and high-brightness gamma rays that are produced by an inverse Compton scattering (ICS) light source provide an ideal probe for gamma-ray imaging. However, owing to the influence of the intrinsic energy-angle correlation spectrum of this type of light source, monochromatic computed tomography (CT), especially in the gamma-ray energy region, can only be realized in a low-efficiency manner, similar to first-generation CT. A dual-energy scan scheme with a large imaging field of view (FOV) was developed in this study to improve the imaging efficiency. The effectiveness of this scheme was demonstrated based on the beam parameters of a typical ICS light source using Monte Carlo simulations. By leveraging the principle of basis material decomposition, the influence of the energy-angle correlation spectrum on CT reconstruction was corrected, and a monochromatic CT image of the imaging object was accurately reconstructed. Furthermore, the electron density and effective atomic number of the imaging object could be obtained simultaneously.

Keywords Gamma-ray computed tomography · Energy-angle correlation · Basis material decomposition · Inverse Compton scattering light source · Monte Carlo simulation

1 Introduction

Since the 1970s, computed tomography (CT) has been developed into a powerful tool for industrial nondestructive testing (NDT), in which the structural integrity of assembled devices is assessed and the quality of manufactured components is inspected. The main focus of NDT applications is qualitative feature recognition (or visualization), such as flaw detection, morphological characterization of internal structures, and material wear inspection. With the development of state-of-the-art precision engineering (e.g., additive manufacturing [1, 2]), there is an increasing demand for accurate dimensional measurements to assure manufacturing quality (e.g., wall thickness, pore size, and geometry tolerance verification) without destroying the part. The CT technique plays a significant role in dimensional metrology [3–6], especially for the dimensional determination of the internal or hidden structures of a component.

In industrial CT systems, X-rays are generally produced by the so-called bremsstrahlung, which is a process in which high-energy electrons are braked by an anode and a continuous spectrum is produced. Because the X-ray absorption of a material is energy dependent, beam-hardening artifacts occur when a polychromatic spectrum is used for CT reconstruction. Owing to the influence of beam-hardening artifacts, serious errors occur in dimensional measurements [7–11], which hamper accurate quantitative analysis and inspection. Since the invention of CT techniques, several methods have been developed to correct this influence. However, those correction algorithms have their own limitations, such as the reduction of photon flux by pre-filtering, the

This work was supported by the National Natural Science Foundation of China (Nos. 12375157, 12027902, and 11905011).

✉ Zhi-Jun Chi
chizj18@bnu.edu.cn

1 Key Laboratory of Beam Technology of Ministry of Education, School of Physics and Astronomy, Beijing Normal University, Beijing 100875, China

2 Key Laboratory of Particle and Radiation Imaging of Ministry of Education, Department of Engineering Physics, Tsinghua University, Beijing 100084, China

requirement of prior knowledge of the imaging materials or spectrum [8, 10, 12–22], two scans at preferably non-overlapping spectra [23, 24], and computational complexity [21, 22, 25–28]. To resolve the beam-hardening effect fundamentally, it is necessary to develop a monochromatic X-ray source, in particular, a monochromatic gamma-ray source with strong penetration power for industrial high-Z material imaging that is characterized by high beam quality, a suitable footprint, and a moderate cost.

With the development of high-brightness electron beams and high-power lasers, the inverse Compton scattering (ICS, also called Thomson scattering in the low-energy region [29, 30]) gamma-ray source has been developed as an excellent light source for advanced gamma-ray imaging because it can provide quasi-monochromatic, continuously energy-tunable, small-focal-spot, and high-brightness gamma rays [31–33]. Furthermore, the footprint of this type of light source is at the room or container scale, making it flexible for clinical or industrial NDT applications. Therefore, ICS light sources have recently attracted significant attention in the field of advanced radiation imaging, including monochromatic and spectral imaging [34–37], phase contrast imaging [38–42], polarization-based imaging [43, 44], and nuclear resonance fluorescence imaging [45–49]. For an ICS light source, the gamma-ray photon energy E_γ in a head-on interaction geometry between the relativistic electron and laser, and considering the relativistic approximation ($\gamma \gg 1$, $\gamma^2 \gg a_0^2$, and $\theta \ll 1$), can be described as [50]

$$E_\gamma = \frac{4\gamma^2 E_\mathrm{l}}{1 + a_0^2/2 + (\gamma\theta)^2}, \tag{1}$$

where E_l is the laser photon energy, γ is the relativistic Lorentz factor, a_0 is the magnitude of the normalized laser vector potential, which can be neglected in the linear scattering process ($a_0 \ll 1$), and θ is the detection angle between the electron moving direction and gamma-ray observation direction. The gamma-ray energy is correlated with the detection angle. The detection angle must be confined by a collimator to obtain quasi-monochromatic gamma rays. Therefore, the field of view (FOV) for imaging is very small, especially in the high-energy region where γ is very large and E_γ is more sensitive to changes in θ. For example, for gamma rays with a peak energy of 2 MeV generated using a laser with a wavelength of 800 nm, the typical FOV within which the gamma-ray bandwidth is determined only by the beam parameters (intrinsic bandwidth, not influenced by the energy-angle correlation) is ~5 mm or less at 10 m downstream of the interaction point (IP) between the relativistic electron and laser. Hence, the "translation + rotation" scan scheme of first-generation CT must be used to realize CT for centimeter-scale objects, which has been proved to be time-consuming.

To improve the imaging efficiency of gamma-ray CT based on ICS light sources, the imaging FOV must be increased without reducing the beam intensity, which means that special efforts must be made to correct the influence of the intrinsic energy-angle correlation spectrum of this type of light source on CT reconstruction. In this study, a dual-energy scan scheme is proposed to realize large-FOV gamma-ray CT by taking full advantage of the straightforward energy tunability of ICS light sources. The feasibility of this scheme was investigated based on a typical ICS light source using Monte Carlo simulations.

2 Methods

2.1 Principle of gamma-ray dual-energy scan scheme

According to the interaction mechanism between X-ray photons and materials, the linear attenuation coefficient $\mu(E)$ of a material can be decomposed into three parts:

$$\mu(E) = a_\mathrm{PE} f_\mathrm{PE}(E) + a_\mathrm{CS} f_\mathrm{CS}(E) + a_\mathrm{PP} f_\mathrm{PP}(E), \tag{2}$$

where $f_\mathrm{PE}(E)$, $f_\mathrm{CS}(E)$, and $f_\mathrm{PP}(E)$ are the energy E dependencies of the photoelectric, Compton scattering, and pair production effects, respectively. The decomposition coefficients a_PE, a_CS, and a_PP are related to the material properties:

$$a_\mathrm{PE} = K_1 Z^n \rho \frac{Z}{A}, \tag{3a}$$

$$a_\mathrm{CS} = K_2 \rho \frac{Z}{A}, \tag{3b}$$

$$a_\mathrm{PP} = K_3 Z \rho \frac{Z}{A}, \tag{3c}$$

where ρ, Z, and A denote the mass density, atomic number, and atomic weight, respectively, K_1, K_2, and K_3 are constants, and $n \approx 3$.

In the low-energy region ($E < 1.022$ MeV), the pair production process cannot occur. Hence, only the photoelectric and Compton scattering terms in Eq. (2) contribute to the linear attenuation coefficient $\mu(E)$. For the photoelectric term, $f_\mathrm{PE}(E)$ is empirically considered as $1/E^3$ when no electron–shell discontinuity occurs in the given energy region, which restricts the model to application to very-high-Z materials. For the Compton scattering term, $f_\mathrm{CS}(E)$ is explicitly described by the well-known Klein–Nishina formula, which assumes the unbound electron and at-rest conditions, neglecting the incoherent scattering function and Doppler broadening, respectively. Using dual-energy CT scans, the projections of a_PE and a_CS can be calculated, based on which the spatial distribution of a_{PE} and a_{CS} can be reconstructed. Thus, a monochromatic CT image of the imaging object can be obtained using Eq. (2) by neglecting the pair production term. This is the principle of the dual-energy method for beam-hardening correction in the diagnostic X-ray energy region [23, 24], which has been applied to energy-angle correlation correction for monochromatic CT based on an ICS light source in the keV energy region [35].

In the high-energy region (e.g., hundreds of keV to several MeVs), the contribution of the photoelectric effect to the linear attenuation coefficient $\mu(E)$ is usually negligible compared with those of the Compton scattering and pair production terms. In principle, the spatial distributions of a_{CS} and a_{PP} for an imaging object can also be reconstructed using a dual-energy scan. However, no explicit expression for $f_{\mathrm{PP}}(E)$ exists owing to the complex energy dependence of the pair production effect. In this case, the basis material decomposition model is often adopted [51].

In the basis material decomposition model, an arbitrary material can be considered as a mixture of two basis materials and its linear attenuation coefficient $\mu(E)$ can be decomposed as

$$\mu(E) = c_1\mu_{\mathrm{BM},1}(E) + c_2\mu_{\mathrm{BM},2}(E), \tag{4}$$

where $\mu_{\mathrm{BM},1}(E)$ and $\mu_{\mathrm{BM},2}(E)$ are the linear attenuation coefficients of the two basis materials, whose values at any gamma-ray energy are known, and c_1 and c_2 are the decomposition coefficients. When a dual-energy scan is performed, the projections of the linear attenuation coefficient at both high and low gamma-ray energies can be obtained as follows:

$$P_{\mathrm{H}} = -\ln\int_{\mathrm{SpecH}} S(E)\exp\left[-\int_s \mu(\vec{r}, E)\mathrm{d}s\right]\mathrm{d}E, \tag{5a}$$

$$P_{\mathrm{L}} = -\ln\int_{\mathrm{SpecL}} S(E)\exp\left[-\int_s \mu(\vec{r}, E)\mathrm{d}s\right]\mathrm{d}E, \tag{5b}$$

where P_{H} and P_{L} are the measured projections at the high-energy spectrum (SpecH) and low-energy spectrum (SpecL), respectively, $\vec{r}$ denotes a position vector in Euclidean space, and $S(E)$ is the intensity-normalized energy spectrum [$\int_{\mathrm{SpecH}} S(E)\mathrm{d}E = 1$ and $\int_{\mathrm{SpecL}} S(E)\mathrm{d}E = 1$], which can be approximated by a Gaussian distribution at any local position of the gamma-ray beam profile for an ICS light source. Because the local bandwidth of an ICS light source is very narrow (the typical rms value is several percent), compared with the energy dependence of $\mu(E)$ in the high-energy region, $S(E)$ can be treated as a Dirac function $\delta(E)$. Thus, Eq. (5) can be further simplified as

$$P_{\mathrm{H}} = \int_s \mu(\vec{r}, E_{\mathrm{H}})\mathrm{d}s, \tag{6a}$$

$$P_{\mathrm{L}} = \int_s \mu(\vec{r}, E_{\mathrm{L}})\mathrm{d}s, \tag{6b}$$

where E_{H} and E_{L} are the peak energies in the high- and low-energy spectra, respectively. By combining Eqs. (4) and (6), the following linear equation system can be established:

$$\begin{bmatrix} P_{\mathrm{H}} \\ P_{\mathrm{L}} \end{bmatrix} = \begin{bmatrix} \mu_{\mathrm{BM},1}(E_{\mathrm{H}}) & \mu_{\mathrm{BM},2}(E_{\mathrm{H}}) \\ \mu_{\mathrm{BM},1}(E_{\mathrm{L}}) & \mu_{\mathrm{BM},2}(E_{\mathrm{L}}) \end{bmatrix} \begin{bmatrix} C_1 \\ C_2 \end{bmatrix}, \tag{7}$$

with

$$C_1 = \int_s c_1(\vec{r})\mathrm{d}s, \tag{8a}$$

$$C_2 = \int_s c_2(\vec{r})\mathrm{d}s. \tag{8b}$$

The projections C_1 and C_2 can be calculated by solving the linear equation system of Eq. (7). Thus, the projection $P(E)$ of the linear attenuation coefficient at an arbitrary energy E can be obtained as follows:

$$P(E) = \int_s \mu(\vec{r}, E)\mathrm{d}s = C_1\mu_{\mathrm{BM},1}(E) + C_2\mu_{\mathrm{BM},2}(E), \tag{9}$$

and the monochromatic CT image of the imaging object at energy E can be obtained by reconstructing $P(E)$.

The gamma-ray energy of an ICS light source can be easily adjusted by changing either the electron energy or interaction angle between the electron and laser. The influence of the energy-angle correlation spectrum encountered in a large-FOV imaging geometry using ICS light sources on CT reconstruction can be easily resolved using a dual-energy scan. Although an energy-angle correlation exists in the scan of each gamma-ray peak energy, the local quasi-monochromaticity [$\delta(E)$ approximation] at an arbitrary detection angle of the FOV (or an arbitrary detection position within the gamma-ray beam profile) can be satisfied (see Sect. 2.2 for the simulated gamma-ray spectra). Hence, two projections at different gamma-ray energies (E_{H} and E_{L}) can be obtained at any detection angle of the FOV. The two gamma-ray energies E_{H} and E_{L} can be calculated using Eq. (1) when the gamma-ray peak energies ($E_{\mathrm{H,max}}$ and $E_{\mathrm{L,max}}$) are determined, based on which the values of $\mu_{\mathrm{BM},1}$ and $\mu_{\mathrm{BM},2}$ can be obtained at the two gamma-ray energies E_{H} and E_{L}. By solving Eq. (7) and using the composition relation in Eq. (9), the projections of the imaging object at any detection angle of the FOV can be corrected to the same gamma-ray energy, as illustrated in Fig. 1. Therefore, a monochromatic CT image of the imaging object can be reconstructed.

2.2 Monte Carlo simulation

Monte Carlo (MC) simulations were performed using the Geant4 toolkit [52] to demonstrate the feasibility of the large-FOV gamma-ray CT scheme. The imaging geometry was modeled based on the imaging system constructed for the very compact ICS gamma-ray source (VIGAS) [53–55] that is under construction at Tsinghua University. A fan beam geometry was adopted, and the imaging layout is illustrated in Fig. 2. Gamma-ray photons were generated from the IP (gamma-ray spot size 10 µm, rms) and propagated $R_1 = 10$ m to the imaging object. The spectrum of the gamma-ray photons, as shown in Fig. 3, was generated from CAIN [56], which is the most commonly used MC code for ICS simulations, by considering the practical beam parameters of the VIGAS. The gamma-ray peak energies $E_{\mathrm{L,max}}$ and $E_{\mathrm{H,max}}$ of the dual-energy scan were 2 and 4 MeV, respectively. The imaging object was scanned separately by the two spectra. At the VIGAS, gamma rays with peak energies of 2 and 4 MeV were generated by the interaction of 290 MeV electrons and lasers with wavelengths of 800 and 400 nm,

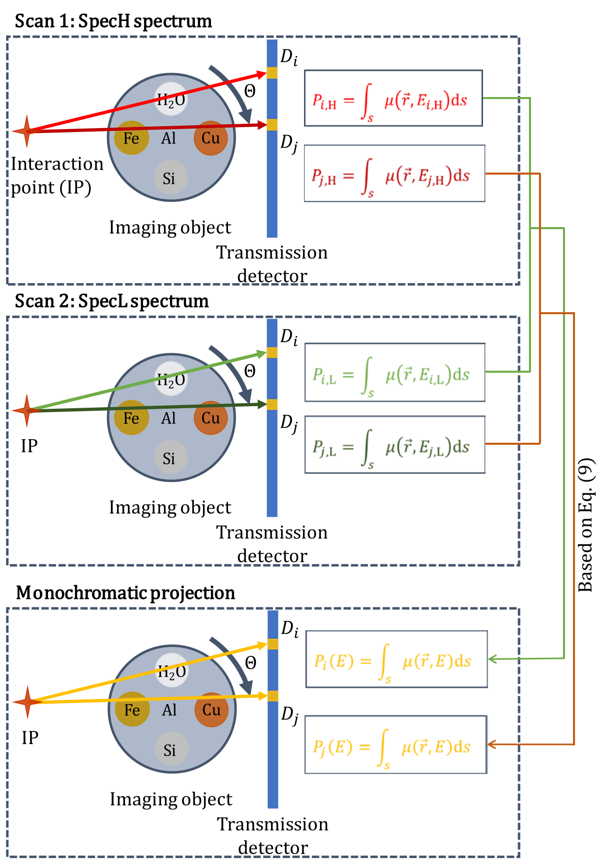

Fig. 1 (Color online) Dual-energy scan scheme for obtaining monochromatic projections of the imaging object at different detector pixels D_i and D_j

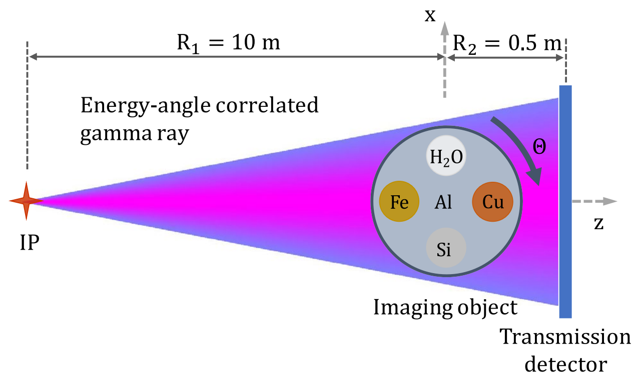

Fig. 2 (Color online) Imaging layout for large-FOV gamma-ray CT based on an ICS light source (not to scale)

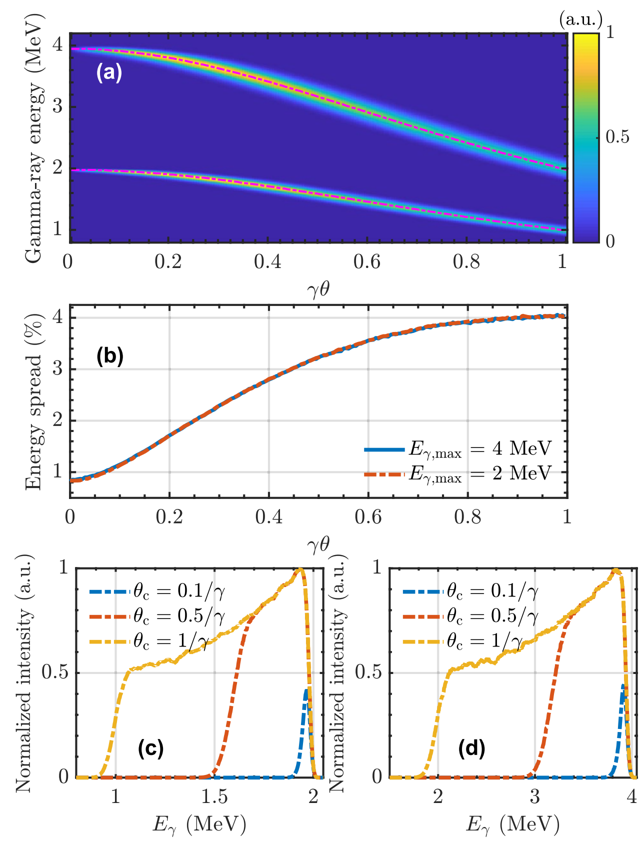

Fig. 3 (Color online) Simulation spectra of the VIGAS using the CAIN software: **a** angular distribution of the generated gamma rays, **b** local rms energy spreads at different detection angles (or different detection positions within the gamma-ray beam profile), and normalized gamma-ray spectra at different collection angles θ_c for $E_{\gamma,\max} = 2$ MeV (**c**) and 4 MeV (**d**), respectively. The pink dotted lines in **a** are the theoretical results obtained from Eq. (1). Although the gamma-ray energy spread increases with the detection angle, the spectrum is still sufficiently narrow that it can be considered to be quasi-monochromatic at different detection angles

respectively. The CAIN simulation results of the gamma-ray spectrum were loaded into Geant4 for further imaging simulations. Both the energy-angle correlation and energy spread of the spectrum were considered in the MC simulation. To acquire the projection data of the imaging object, an ideal transmission detector with a pixel size of 0.2 mm was placed $R_2 = 0.5$ m downstream of the imaging object. The photon intensity of the generated gamma rays of an ICS light source decreases with the detection angle, as shown in Fig. 3a. To guarantee the necessary photon intensity at the boundary of the gamma-ray beam profile, the gamma-ray collection angle θ_c was selected as $1/\gamma$ (~1.76 mrad), which corresponds to an FOV of ~3.5 cm at the position of the imaging object. Compared with the quasi-monochromatic case (typical FOV of ~5 mm or less at 2 MeV), the FOV increases more than sevenfold in the dual-energy scan scheme.

The imaging object was an aluminum (Al) cylinder with a diameter of 3.0 cm, inside which there were four cylindrical columns with a diameter of 8.0 mm. The four inner columns were made of iron (Fe), copper (Cu), water (H_2O), and silicon (Si), respectively. For the CT scan of the imaging object, the rotation axis was the central axis of the Al cylinder, located at the center of the gamma-ray beam.

In the MC simulation, 360 projections that were evenly distributed in the angular range of 0–360° were acquired for each CT scan. In each projection, 9×10^7 gamma-ray photons were simulated to balance the statistical error and time cost.

2.3 Image reconstruction

Based on the dual-energy scan scheme, the monochromatic projections of the imaging object at an arbitrary gamma-ray energy E could be obtained using Eq. (9). Monochromatic CT reconstruction of the imaging object at gamma-ray energies of 2 and 4 MeV was realized using the well-known ART-TV iterative algorithm.

Because monochromatic CT images of the imaging object at gamma-ray energies of 4 and 2 MeV were obtained, the effective atomic number Z_{eff} and electron density ρ_e of the imaging object could also be obtained. By combining Eqs. (2) and (3), the linear attenuation coefficient of a material in the gamma-ray energy region can be expressed as

$$\mu(E) = g_2 \rho_e f_{\mathrm{CS}}(E) + g_3 Z_{\mathrm{eff}} \rho_e f_{\mathrm{PP}}(E), \tag{10}$$

where g_2 and g_3 are constants related to K_2 and K_3, respectively, and ρ_e is defined as

$$\rho_e = \rho \frac{Z}{A} N_A, \tag{11}$$

where N_A is Avogadro's constant. Furthermore, considering the basis material decomposition model in Eq. (4), the electron density ρ_e and effective atomic number Z_{eff} of a material can be expressed as

$$\rho_e = c_1 \rho_{e,1} + c_2 \rho_{e,2}, \tag{12a}$$

$$Z_{\mathrm{eff}} = \frac{c_1 Z_1 \rho_{e,1} + c_2 Z_2 \rho_{e,2}}{\rho_e}, \tag{12b}$$

where Z_i and $\rho_{e,i}$ ($i = 1$ or 2) are the known atomic number and electron density of the ith basis material, respectively. To obtain ρ_e and Z_{eff}, the values of c_1 and c_2 are required, which can be calculated by directly reconstructing Eq. (8) or by solving Eq. (4) at two different gamma-ray energies. Distinguished by whether $\mu(E)$ reconstruction is required, the reconstruction of c_1 and c_2 can be realized using either pre- or post-processing methods. In the preprocessing method, c_1 and c_2 are reconstructed based on the projection data C_1 and C_2 calculated by solving Eq. (7). In the post-processing method, a monochromatic CT image of the imaging object should first be reconstructed at two different gamma-ray energies, E_H (e.g., 4 MeV) and E_L (e.g., 2 MeV), following which c_1 and c_2 can be calculated by solving Eq. (4) at the two gamma-ray energies E_H and E_L.

3 Results and discussion

The basis materials selected for the CT reconstruction of the imaging object were iron (Fe) and carbon (C), the linear attenuation coefficients of which can be found in the National Institute of Standards and Technology (NIST) [57]. The CT reconstruction results of the imaging object using the original energy-angle correlation spectrum with a gamma-ray peak energy of 2 MeV and the monochromatic CT reconstruction results at a gamma-ray energy of 2 MeV using the dual-energy scan scheme are illustrated in Fig. 4a and b, respectively. To avoid the mosaic phenomenon in the CT reconstruction image caused by undersampling and to obtain a smooth reconstruction result, 512×512 pixels were selected in the CT reconstruction region, which led to a virtual resolution that was much higher than the practical resolution of the transmission detector. The horizontal and vertical center profiles of the reconstruction results are shown in Fig. 4c and d, respectively, to provide a quantitative comparison. Similar CT reconstruction results at a gamma-ray energy of 4 MeV are illustrated in Fig. 5. Owing to the influence of the energy-angle correlation spectra, obvious "cupping artifacts" appeared in the reconstructed images. Using the dual-energy scan scheme described in Sect. 2.1, the "cupping artifacts" could be perfectly corrected, and the reconstructed linear attenuation coefficient of the imaging object agreed well with its theoretical value, as shown

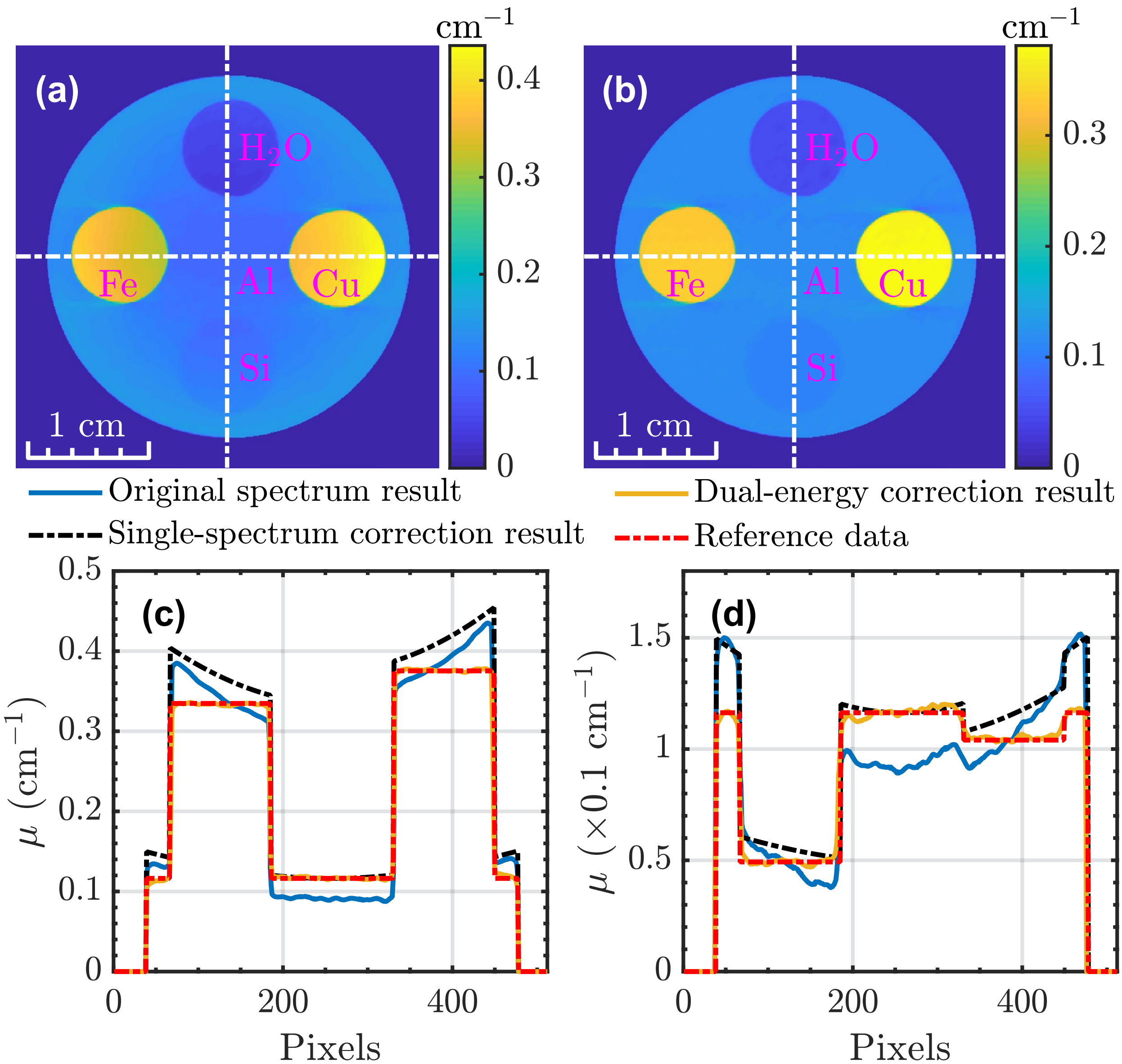

Fig. 4 (Color online) CT reconstruction results of the imaging object: **a** direct reconstruction using the original energy-angle correlation spectrum at a gamma-ray peak energy of 2 MeV; **b** monochromatic reconstruction at a gamma-ray energy of 2 MeV using the dual-energy scan scheme; and **c** and **d** horizontal and vertical center profiles [white dotted lines in **a** and **b**] of the reconstruction images, respectively

in Figs. 4c, 4d, 5c, and 5d. Considering that gamma-ray energy is correlated with the detection angle, different parts of the imaging object are irradiated by gamma rays with different energies. The energy-modified linear attenuation coefficient of the imaging object, which yields the theoretical $\mu(E)$ of the imaging object with the gamma-ray energy E calculated based on the energy-angle correlation relation in Eq. (1), is also illustrated in Figs. 4c, 4d, 5c, and 5d using black dotted lines. The energy-modified linear attenuation coefficient of the imaging object exhibited a similar variation tendency to the reconstruction result using the original energy-angle correlation spectrum, in which the linear attenuation coefficient for the same material increased with the radius. However, a quantitative comparison shows that the two results do not agree well, particularly around the center of the imaging object. Therefore, the single-spectrum correction using the energy-angle correlation information in Eq. (1) cannot reflect the practical reconstruction results.

The electron density and effective atomic number of the imaging object reconstructed using the pre- and post-processing methods are shown in Figs. 6 and 7, respectively. For

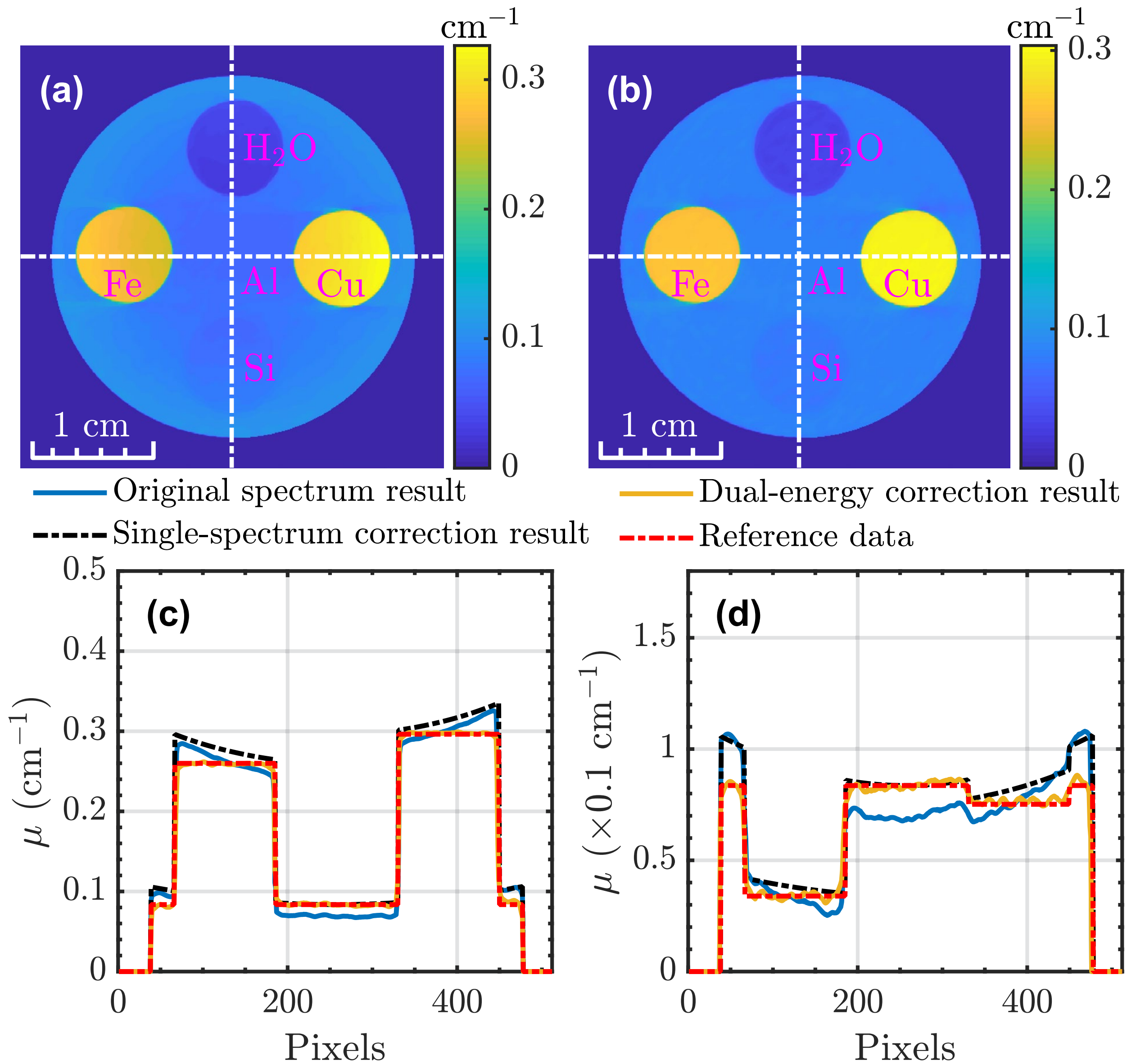

Fig. 5 (Color online) CT reconstruction results of the imaging object: **a** direct reconstruction using the original energy-angle correlation spectrum at a gamma-ray peak energy of 4 MeV; **b** monochromatic reconstruction at a gamma-ray energy of 4 MeV using the dual-energy scan scheme; and **c** and **d** horizontal and vertical center profiles [white dotted lines in **a** and **b**] of the reconstruction images, respectively

both reconstruction methods, the reconstruction quality of the electron density was much better than that of the effective atomic number, which can be attributed to the division operation in Eq. (12b). Compared with the preprocessing method, there were serious artifacts around the boundaries of H_2O, Fe, and Cu in the Z_{eff} image reconstructed using the post-processing method.

To evaluate the reconstruction quality of the two methods quantitatively, five regions of interest (ROIs) were selected, as indicated by the white dotted squares in Figs. 6a, 6d, 7a, and 7d. The ρ_e and Z_{eff} reconstruction results for the five materials are presented in Tables 1 and 2, respectively. Both the mean value and its standard error calculated over the ROIs are provided for the reconstructed values in Tables 1 and 2. In terms of ρ_e, the precision (standard error) of the five materials reconstructed using the post-processing method was much higher than the value using the preprocessing method. Meanwhile, the accuracy (relative error) of ρ_e reconstructed using the post-processing method was slightly higher than the value using the preprocessing method for all materials, except for Cu. In terms of Z_{eff}, the reconstruction precision using the post-processing method

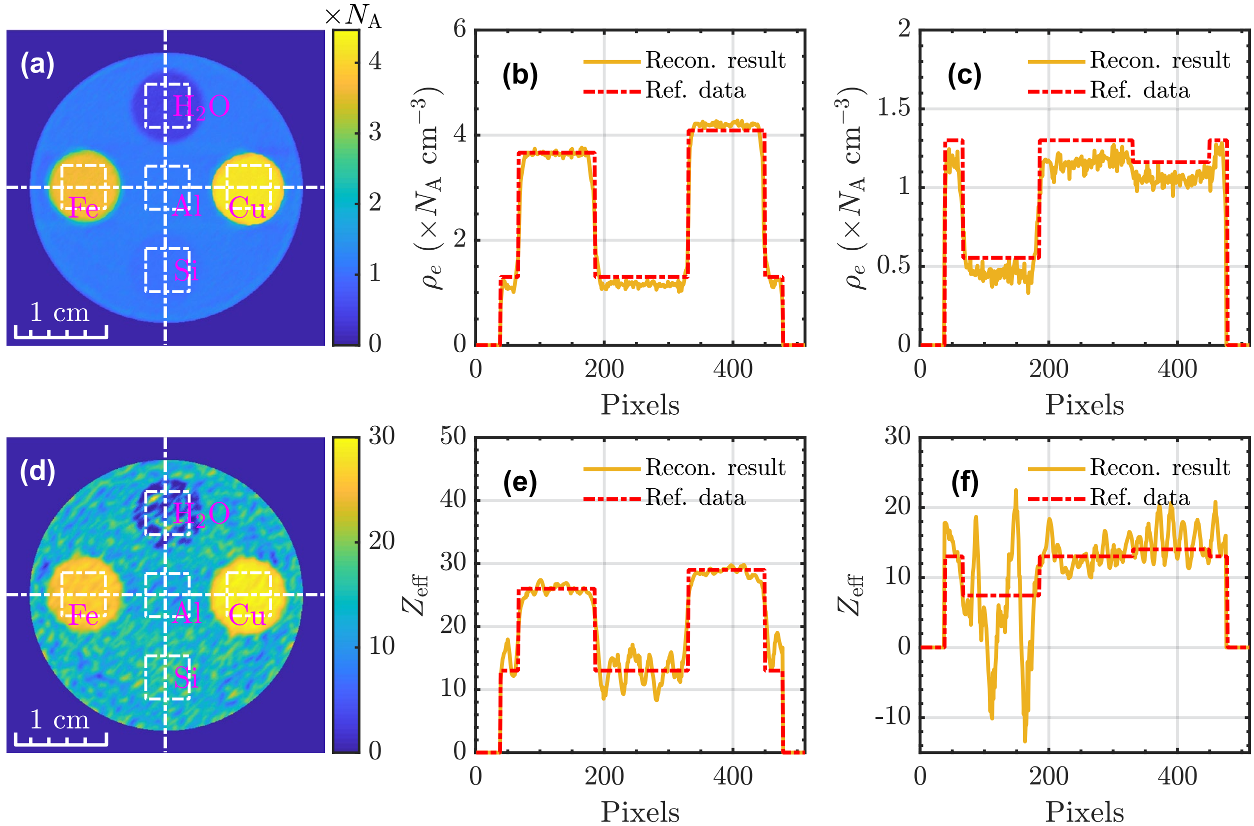

Fig. 6 (Color online) Electron density and effective atomic number of the imaging object reconstructed using the preprocessing method: **a** ρ_e image; **b** and **c** horizontal and vertical center profiles of **a**, respectively; **d** Z_{eff} image; and **e** and **f** horizontal and vertical center profiles of **d**, respectively. The white dotted squares in **a** and **d** are ROIs selected for quantitative analysis of the reconstruction results

was slightly lower than that using the preprocessing method for all materials except for H_2O, and the reconstruction accuracy using the post-processing method was similar to that using the preprocessing method for all materials except for H_2O. Therefore, the post-processing method is more suitable for ρ_e reconstruction, whereas the preprocessing method is more suitable for Z_{eff} reconstruction. For moderate-Z materials (e.g., Fe and Cu), excellent reconstruction was obtained, with accuracies of less than 3% and 1.5% for ρ_e and Z_{eff}, respectively. For Fe, the relative errors of ρ_e and Z_{eff} were the smallest, which was expected because Fe is a basis material. For relatively low-Z materials (e.g., Al, Si, and H_2O), the lower ρ_e reconstruction accuracy may be attributed to the less accurate basis material decomposition of the linear attenuation coefficient. Basis material decomposition models with higher accuracy must be developed in future studies to improve the reconstruction accuracy of ρ_e. In addition, the gamma-ray energy selected for the dual-energy scan may be a reason for the high relative errors of the ρ_e and Z_{eff} reconstruction for these low-Z materials. Because gamma-ray energies of 2 and 4 MeV are too high for low-Z materials in the imaging object, the statistical error of the monochromatic CT reconstruction was relatively high, as shown in Figs. 4d and 5d, which resulted in a high relative error in the ρ_e and Z_{eff} reconstruction. To reduce the relative errors of ρ_e and Z_{eff} caused by the selection of gamma-ray energy for the dual-energy scan, the photon number used for the MC simulation should be increased or the gamma-ray energy should be reduced. Although the preprocessing method for Z_{eff} reconstruction has advantages over the post-processing method in terms of boundary artifact suppression and high-precision reconstruction, the reconstruction precision of Z_{eff} owing to the division operation in Eq. (12b) was significantly lower than that of ρ_e. Therefore, effective reconstruction methods must be developed to improve the reconstruction precision of Z_{eff}.

Because the FOV using the dual-energy scan scheme is increased by more than sevenfold compared with the quasi-monochromatic scan ("translation + rotation" scheme), the imaging time using the dual-energy scan scheme (only "rotation" is required) when CT scans using different gamma-ray energies are carried out separately can be reduced by at least 3.5 times. However, dual-color gamma rays can be easily produced simultaneously for an ICS light source [58–60] using one of the following three schemes: (i) dual-color lasers interacting with the same electron beam, (ii) a

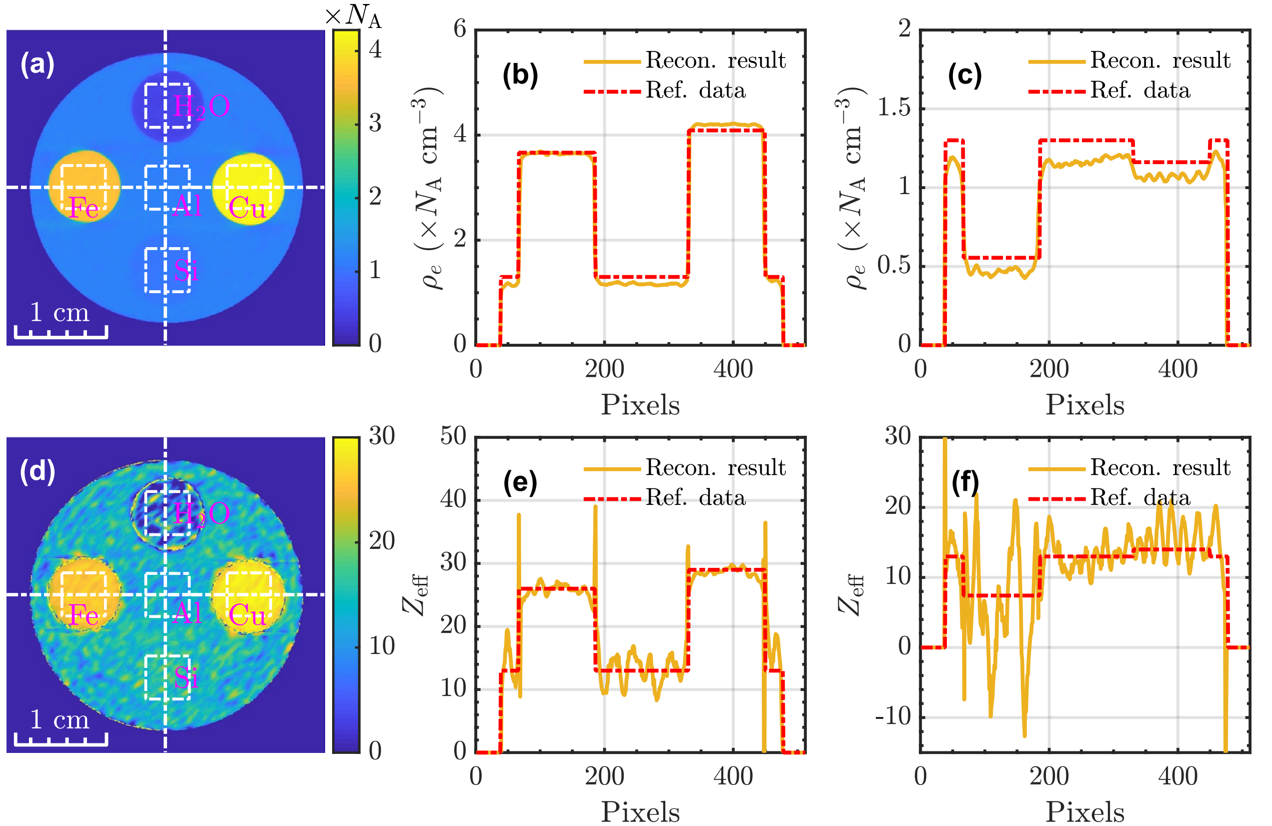

Fig. 7 (Color online) Electron density and effective atomic number of the imaging object reconstructed using the post-processing method: **a** ρ_e image; **b** and **c** horizontal and vertical center profiles of **a**, respectively; **d** Z_{eff} image; and **e** and **f** horizontal and vertical center profiles of **d**, respectively. The white dotted squares in **a** and **d** are ROIs selected for quantitative analysis of the reconstruction results

Table 1 Reconstructed electron density ρ_e of the imaging object

Material	Reference value ($\times N_A$ cm^{-3})	Preprocessing		Post-processing	
		Reconstruction value ($\times N_A$ cm^{-3})	Relative error (%)	Reconstruction value ($\times N_A$ cm^{-3})	Relative error (%)
Al	1.300	1.159±0.097	10.89	1.164±0.023	10.47
Si	1.162	1.053±0.092	9.35	1.063±0.016	8.50
H_2O	0.555	0.461±0.099	16.92	0.470±0.020	15.35
Fe	3.666	3.651±0.088	0.42	3.654±0.023	0.32
Cu	4.089	4.196±0.093	2.62	4.198±0.023	2.67

Table 2 Reconstructed effective atomic number Z_{eff} of the imaging object

Material	Reference value	Preprocessing		Post-processing	
		Reconstruction value	Relative error (%)	Reconstruction value	Relative error (%)
Al	13	12.58±2.69	3.21	12.66±2.88	2.58
Si	14	15.39±2.50	9.91	15.42±2.78	10.16
H_2O	7.42	6.54±9.01	11.83	7.14±8.65	3.74
Fe	26	25.94±0.79	0.26	25.93±0.82	0.28
Cu	29	28.68±0.76	1.09	28.69±0.78	1.07

single-color laser interacting with the same electron beam at different interaction angles by beam splitting, and (iii) dual-color electron beams interacting with the same laser. Using dual-color gamma rays, a dual-energy scan can be realized simultaneously by combining it with a layered transmission detector (the front layer for low-energy gamma-ray detection and the rear layer for high-energy gamma-ray detection, as in the case of early dual-energy CT [61, 62]). Therefore, the imaging time can be reduced further by 2 times. Another advantage of the dual-energy scan scheme compared with the quasi-monochromatic scan is that the ρ_e and Z_{eff} of the imaging object can be obtained simultaneously.

4 Conclusion

Quasi-monochromatic, continuously energy-tunable, and high-brightness gamma rays produced by ICS light sources can fundamentally resolve beam-hardening artifacts in CT reconstruction, which can improve the accuracy of quantitative analysis and inspection in CT-based dimensional metrology. An effective method for large-FOV imaging was developed to improve the imaging efficiency of gamma-ray CT using this type of light source. Using a dual-energy scan scheme, the influence of the intrinsic energy-angle correlation spectrum of ICS light sources on CT reconstruction was resolved, and a monochromatic CT image of the imaging object was accurately reconstructed. Furthermore, the electron density ρ_e and effective atomic number Z_{eff} of the imaging object were obtained. For ρ_e reconstruction, the post-processing method has an obvious advantage over the preprocessing method; however, for Z_{eff} reconstruction, the preprocessing method is preferred.

Author contributions All authors contributed to the study conception and design. Material preparation, data collection, and analysis were performed by Zhi-Jun Chi, Hong-Ze Zhang, Jia-Yi Sun, Hao Ding, Jin Lin, Xuan-Qi Zhang, and Qi-Li Tian. The first draft of the manuscript was written by Zhi-Jun Chi, and all authors commented on previous versions of the manuscript. All authors read and approved the final manuscript.

Data availability The data that support the findings of this study are openly available in Science Data Bank at https://cstr.cn/31253.11.sciencedb.j00186.00960 and https://www.doi.org/ 10.57760/sciencedb.j00186.00960.

Declarations

Conflict of interest The authors declare that they have no conflict of interest.

References

1. K.V. Wong, A. Hernandez, A review of additive manufacturing. Int. Sch. Res. Not. **2012**, 208760 (2012). https://doi.org/10.5402/2012/208760
2. W. Gao, Y.B. Zhang, D. Ramanujan et al., The status, challenges, and future of additive manufacturing in engineering. Comput. Aided Des. **69**, 65–89 (2015). https://doi.org/10.1016/j.cad.2015.04.001
3. J.P. Kruth, M. Bartscher, S. Carmignato et al., Computed tomography for dimensional metrology. CIRP Ann. Manuf. Technol. **60**, 821–842 (2011). https://doi.org/10.1016/j.cirp.2011.05.006
4. L. De Chiffre, S. Carmignato, J.P. Kruth et al., Industrial applications of computed tomography. CIRP Ann. Manuf. Technol. **63**, 655–677 (2014). https://doi.org/10.1016/j.cirp.2014.05.011
5. M. Ferrucci, R.K. Leach, C. Giusca et al., Towards geometrical calibration of X-ray computed tomography—a review. Meas. Sci. Technol. **26**, 092003 (2015). https://doi.org/10.1088/0957-0233/26/9/092003
6. H. Villarraga-Gómez, E.L. Herazo, S.T. Smith, X-ray computed tomography: from medical imaging to dimensional metrology. Precis. Eng. **60**, 544–569 (2019). https://doi.org/10.1016/j.precisioneng.2019.06.007
7. M. Bartscher, U. Hilpert, J. Goebbels et al., Enhancement and proof of accuracy of industrial computed tomography (CT) measurements. CIRP Ann. **56**, 495–498 (2007). https://doi.org/10.1016/j.cirp.2007.05.118
8. W. Dewulf, Y. Tan, K. Kiekens, Sense and non-sense of beam hardening correction in CT metrology. CIRP Ann. Manuf. Technol. **61**, 495–498 (2012). https://doi.org/10.1016/j.cirp.2012.03.013
9. X. Zhang, L. Li, F. Zhang et al., Improving the accuracy of CT dimensional metrology by a novel beam hardening correction method. Meas. Sci. Technol. **26**, 015007 (2014). https://doi.org/10.1088/0957-0233/26/1/015007
10. Y. Tan, K. Kiekens, F. Welkenhuyzen et al., Simulation-aided investigation of beam hardening induced errors in CT dimensional metrology. Meas. Sci. Technol. **25**, 064014 (2014). https://doi.org/10.1088/0957-0233/25/6/064014
11. J.J. Lifton, A.A. Malcolm, J.W. McBride, An experimental study on the influence of scatter and beam hardening in X-ray CT for dimensional metrology. Meas. Sci. Technol. **27**, 015007 (2015). https://doi.org/10.1088/0957-0233/27/1/015007
12. G.T. Herman, Correction for beam hardening in computed tomography. Phys. Med. Biol. **24**, 81 (1979). https://doi.org/10.1088/0031-9155/24/1/008
13. H.W. Gao, L. Zhang, Z.Q. Chen et al., Beam hardening correction for middle-energy industrial computerized tomography. IEEE Trans. Nucl. Sci. **53**, 2796–2807 (2006). https://doi.org/10.1109/TNS.2006.879825
14. X.Q. Mou, S.J. Tang, H.Y. Yu, A beam hardening correction method based on HL consistency. Proc. SPIE **6318**, 583–592 (2006). https://doi.org/10.1117/12.682869
15. Y.B. Zhang, X.Q. Mou, S.J. Tang, Beam hardening correction for fan-beam CT imaging with multiple materials. IEEE Nuclear Science Symposium & Medical Imaging Conference, Knoxville, TN, USA, 2010, 3566–3570 (2010). https://doi.org/10.1109/NSSMIC.2010.5874473
16. S.J. Tang, X.Q. Mou, Q. Xu et al., Data consistency condition-based beam-hardening correction. Opt. Eng. **50**, 076501 (2011). https://doi.org/10.1117/1.3599869
17. S.J. Tang, K.D. Huang, Y.Y. Cheng et al., Optimization based beam-hardening correction in CT under data integral invariant constraint. Phys. Med. Biol. **63**, 135015 (2018). https://doi.org/10.1088/1361-6560/aaca14

18. W. Zhao, G.T. Fu, C.L. Sun et al., Beam hardening correction for a cone-beam CT system and its effect on spatial resolution. Chin. Phys. C **35**, 978 (2011). https://doi.org/10.1088/1674-1137/35/10/018
19. S.H. Luo, H.Z. Wu, Y. Sun et al., A fast beam hardening correction method incorporated in a filtered back-projection based MAP algorithm. Phys. Med. Biol. **62**, 1810 (2017). https://doi.org/10.1088/1361-6560/aa56b5
20. M. Kachelrieß, K. Sourbelle, W.A. Kalender, Empirical cupping correction: A first-order raw data precorrection for cone-beam computed tomography. Med. Phys. **33**, 1269–1274 (2006). https://doi.org/10.1118/1.2188076
21. M. Abella, C. Martínez, M. Desco et al., Simplified statistical image reconstruction for X-ray CT with beam-hardening artifact compensation. IEEE Trans. Med. Imaging **39**, 111–118 (2019). https://doi.org/10.1109/TMI.2019.2921929
22. J.A. O'Sullivan, J. Benac, Alternating minimization algorithms for transmission tomography. IEEE Trans. Med. Imaging **26**, 283–297 (2007). https://doi.org/10.1109/TMI.2006.886806
23. R. Alvarez, A. Macowski, Energy-selective reconstructions in x-ray computerized tomography. Phys. Med. Biol. **21**, 733–744 (1976). https://doi.org/10.1088/0031-9155/21/5/002
24. J.P. Stonestrom, R.E. Alvarez, A. Macovski, A framework for spectral artifact corrections in X-ray CT. IEEE Trans. Biomed. Eng. **2**, 128–141 (1981). https://doi.org/10.1109/TBME.1981.324786
25. Y. Censor, T. Elfving, G.T. Herman et al., A method of iterative data refinement and its applications. Math. Methods Appl. Sci. **7**, 108–123 (1985). https://doi.org/10.1002/mma.1670070108
26. J. Hsieh, R.C. Molthen, C.A. Dawson et al., An iterative approach to the beam hardening correction in cone beam CT. Med. Phys. **27**, 23–29 (2000). https://doi.org/10.1118/1.598853
27. G. Van Gompel, K. Van Slambrouck, M. Defrise et al., Iterative correction of beam hardening artifacts in CT. Med. Phys. **38**, S36–S49 (2011). https://doi.org/10.1118/1.3577758
28. L. Brabant, E. Pauwels, M. Dierick et al., A novel beam hardening correction method requiring no prior knowledge, incorporated in an iterative reconstruction algorithm. NDT E Int. **51**, 68–73 (2012). https://doi.org/10.1016/j.ndteint.2012.07.002
29. C.X. Tang, W.H. Huang, R.K. Li et al., Tsinghua Thomson scattering X-ray source. Nucl. Instrum. Methods Phys. Res. Sect. A **608**, S70–S74 (2009). https://doi.org/10.1016/j.nima.2009.05.088
30. X.C. Lin, H. Zha, J.R. Shi et al., Development of a seven-cell S-band standing-wave RF-deflecting cavity for Tsinghua Thomson scattering X-ray source. Nucl. Sci. Tech. **32**, 36 (2021). https://doi.org/10.1007/s41365-021-00871-5
31. H.W. Wang, G.T. Fan, L.X. Liu et al., Commissioning of laser electron gamma beamline SLEGS at SSRF. Nucl. Sci. Tech. **33**, 87 (2022). https://doi.org/10.1007/s41365-022-01076-0
32. X. Pang, B.H. Sun, L.H. Zhu et al., Progress of photonuclear cross sections for medical radioisotope production at the SLEGS energy domain. Nucl. Sci. Tech. **34**, 187 (2023). https://doi.org/10.1007/s41365-023-01339-4
33. L.X. Liu, H.W. Wang, G.T. Fan et al., The SLEGS beamline of SSRF. Nucl. Sci. Tech. **35**, 111 (2024). https://doi.org/10.1007/s41365-024-01469-3
34. K. Achterhold, M. Bech, S. Schleede et al., Monochromatic computed tomography with a compact laser-driven X-ray source. Sci. Rep. **3**, 1313 (2013). https://doi.org/10.1038/srep01313
35. Z.J. Chi, Y.C. Du, W.H. Huang et al., Energy-angle correlation correction algorithm for monochromatic computed tomography based on Thomson scattering X-ray source. J. Appl. Phys. **122**, 234903 (2017). https://doi.org/10.1063/1.4996324
36. Z.J. Chi, Y.C. Du, L.X. Yan et al., Experimental feasibility of dual-energy computed tomography based on the Thomson scattering X-ray source. J. Synchrotron Radiat. **25**, 1797–1802 (2018). https://doi.org/10.1107/S1600577518012663
37. S. Kulpe, M. Dierolf, B. Günther et al., Spectroscopic imaging at compact inverse Compton X-ray sources. Phys. Med. **79**, 137–144 (2020). https://doi.org/10.1016/j.ejmp.2020.11.015
38. M. Bech, O. Bunk, C. David et al., Hard X-ray phase-contrast imaging with the Compact Light Source based on inverse Compton X-rays. J. Synchrotron Radiat. **16**, 43–47 (2009). https://doi.org/10.1107/S090904950803464X
39. E. Eggl, S. Schleede, M. Bech et al., X-ray phase-contrast tomography with a compact laser-driven synchrotron source. Proc. Natl. Acad. Sci. **112**, 5567–5572 (2015). https://doi.org/10.1073/pnas.1500938112
40. Z. Zhang, Y.C. Du, L.X. Yan et al., In-line phase-contrast imaging based on Tsinghua Thomson scattering X-ray source. Rev. Sci. Instrum. **85**, 083307 (2014). https://doi.org/10.1063/1.4893658
41. Z.J. Chi, L.X. Yan, Y.C. Du et al., Recent progress of phase-contrast imaging at Tsinghua Thomson-scattering X-ray source. Nucl. Instrum. Methods Phys. Res., Sect. B **402**, 364–369 (2017). https://doi.org/10.1016/j.nimb.2017.02.062
42. J.Y. Sun, Z.J. Chi, Y.C. Du et al., A simulation method of gamma-ray phase contrast imaging for metal samples. Nucl. Instrum. Methods Phys. Res. Sect. A **1053**, 168321 (2023). https://doi.org/10.1016/j.nima.2023.168321
43. Z.J. Chi, Y.C. Du, W.H. Huang et al., Linearly polarized X-ray fluorescence computed tomography based on a Thomson scattering light source: a Monte Carlo study. J. Synchrotron Radiat. **27**, 737–745 (2020). https://doi.org/10.1107/S1600577520003574
44. Y. Taira, S. Endo, S. Kawamura et al., Measurement of the spatial polarization distribution of circularly polarized gamma rays produced by inverse Compton scattering. Phys. Rev. A **107**, 063503 (2023). https://doi.org/10.1103/PhysRevA.107.063503
45. H.S. Zen, H. Ohgaki, Y. Taira et al., Demonstration of tomographic imaging of isotope distribution by nuclear resonance fluorescence. AIP Adv. **9**, 035101 (2019). https://doi.org/10.1063/1.5064866
46. K. Ali, H. Ohgaki, H.S. Zen et al., Selective isotope CT imaging based on nuclear resonance fluorescence transmission method. IEEE Trans. Nucl. Sci. **67**, 1976–1984 (2020). https://doi.org/10.1109/TNS.2020.3004565
47. H.Y. Lan, T. Song, Z.H. Luo et al., Isotope-sensitive imaging of special nuclear materials using computer tomography based on scattering nuclear resonance fluorescence. Phys. Rev. Appl. **16**, 054048 (2021). https://doi.org/10.1103/PhysRevApplied.16.054048
48. H.Y. Lan, T. Song, J.L. Zhang et al., Rapid interrogation of special nuclear materials by combining scattering and transmission nuclear resonance fluorescence spectroscopy. Nucl. Sci. Tech. **32**, 84 (2021). https://doi.org/10.1007/s41365-021-00914-x
49. M. Omer, T. Shizuma, R. Hajima et al., Nondestructive determination of isotopic abundance using multi-energy nuclear resonance fluorescence driven by laser Compton scattering source. J. Appl. Phys. **135**, 184903 (2024). https://doi.org/10.1063/5.0197076
50. S.K. Ride, E. Esarey, M. Baine, Thomson scattering of intense lasers from electron beams at arbitrary interaction angles. Phys. Rev. E **52**, 5425 (1995). https://doi.org/10.1103/PhysRevE.52.5425
51. Y.X. Xing, L. Zhang, X.H. Duan et al., A reconstruction method for dual high-energy CT with MeV X-rays. IEEE Trans. Nucl. Sci. **58**, 537–546 (2011). https://doi.org/10.1109/TNS.2011.2112779
52. S. Agostinelli, J. Allison, K.A. Amako et al., GEANT4—a simulation toolkit. Nucl. Instrum. Methods Phys. Res. Sect. A **506**, 250 (2003). https://doi.org/10.1016/S0168-9002(03)01368-8
53. Y.C. Du, H. Chen, H.Z. Zhang et al., A very compact inverse Compton scattering gamma-ray source. High Power Laser Part.

Beams **34**, 104010 (2022). https://doi.org/10.11884/HPLPB202234.220132
54. X.C. Lin, H. Zha, J.R. Shi et al., Design, fabrication, and testing of low-group-velocity S-band traveling-wave accelerating structure. Nucl. Sci. Tech. **33**, 147 (2022). https://doi.org/10.1007/s41365-022-01124-9
55. Q. Gao, H. Zha, J.R. Shi et al., Design and test of an X-band constant gradient structure. Phys. Rev. Accel. Beams **27**, 090401 (2024). https://doi.org/10.1103/PhysRevAccelBeams.27.090401
56. CAIN, Version 2.42, https://www-jlc.kek.jp/~tauchi/index/cain/non-linearQED/CainMan242.pdf (last accessed March 29, 2024)
57. X-Ray Mass Attenuation Coefficients, https://www.nist.gov/pml/x-ray-mass-attenuation-coefficients (last accessed April 9, 2024)
58. V. Petrillo, A. Bacci, C. Curatolo et al., Dual color X rays from Thomson or Compton sources. Phys. Rev. ST Accel. Beams **17**, 020706 (2014). https://doi.org/10.1103/PhysRevSTAB.17.020706
59. I. Drebot, V. Petrillo, L. Serafini, Two-colour X-gamma ray inverse Compton back-scattering source. EPL **120**, 14002 (2017). https://doi.org/10.1209/0295-5075/120/14002
60. Y. Wu, C.H. Yu, Z.Y. Qin et al., Dual-color γ-rays via all-optical Compton scattering from a cascaded laser-driven wakefield accelerator. Plasma Phys. Control. Fusion **61**, 085030 (2019). https://doi.org/10.1088/1361-6587/ab29d9
61. T. Ishigaki, S. Sakuma, M. Ikeda, One-shot dual-energy subtraction chest imaging with computed radiography: clinical evaluation of film images. Radiology **168**, 67–72 (1988). https://doi.org/10.1148/radiology.168.1.3289096
62. B.K. Stewart, H.K. Huang, Single-exposure dual-energy computed radiography. Med. Phys. **17**, 866–875 (1990). https://doi.org/10.1118/1.596479